RSC Advances

ROYAL SOCIETY OF CHEMISTRY

www.rsc.org/advances

Quantum confined CdS inclusion in graphene oxide for improved electrical conductivity and facile charge transfer in hetero-junction solar cell

N. Rajeswari Yogamalar,[a] K. Sadhanandam,[a] A. Chandra Bose[b] and R. Jayavel*[a]

[a]*Centre for Nanoscience and Technology, Anna University, Chennai 600025, India*. Email: rjvel@annauniv.edu

[b]*Nanomaterials Laboratory, Department of Physics, National Institute of Technology, Tiruchirappalli 620015, India*

We employed a simple mechanism in tuning the electrical conductivity of graphene oxide (GO) by the inclusion of nano cadmium sulphide (CdS) and thereby, utilizing in *pn* hetero-junction based solar cell. Two different kinds of hetero-junction solar cell devices are fabricated; one with CdS acting as a separate buffer layer in GO and in another, the GO was functionalized with quantum confined CdS particles. In both the kinds, the *n*-type junction was interfaced with the *p*-type semiconductor Rose Bengal (RB). The nano CdS has the ability to harvest useful spectral range of the solar spectrum and to retard the recombination rate between the junction interfaces and hence, promote the facile charge carrier transport within the device. The CdS functionalized GO exhibited a remarkable short circuit current density (J_{sc}) of 4 mA/cm^2, open circuit voltage (V_{oc}) of 685 mV, giving rise to an enhanced power conversion efficiency (η) of 1.97% in comparison to the planar GO hetero-junction. The enhancement in power conversion efficiency and the influence of nano CdS inclusion is analyzed and interpreted on the basis of the electrical studies performed with cyclic voltammetry (CV) and electrical impedance spectroscopy (EIS). From the electrical measurements, the charge storage capacitance of 138 Fg^{-1} and the minimal resistance of 440 Ω are incurred in GO/CdS nanocomposites. The obtained results are further supported by the various physio-chemical characterizations such as X-ray diffraction (XRD), thermogravimetri analysis (TGA), Fourier transform infra red spectroscopy (FTIR), scanning electron microscopy (SEM), transmission electron microscopy (TEM), absorption and luminescence emission studies and demonstrate their significance in photovoltaic application.

Keywords: Quantum confined particles, *pn* hetero-junction, interface, solar spectrum, power conversion efficiency, charge storage capacitance.

Introduction

Innovative research on carbon based nanomaterials has grown rapidly since the experimental discovery of graphene in 2004 through the mechanical exfoliation of graphite [1].

The growth is progressive due to the special chemistry possessed by the graphene an allotrope of carbon material with one-atom thick and two dimensional (2D) conjugated honeycomb lattice structure [2]. The graphene oxide (GO) another form of carbon material is prepared by the oxidation of 3D graphite crystals using strong oxidizing agents. The oxygenated functional groups such as carboxyl group (O=C-OH) at the edges, hydroxyl group (-OH) and epoxy group (-C-O-C-) at the basal plane enable the GO to be stacked one on each other to form extremely thin and mechanically strong layer [3]. As they are bonded covalently with the oxygenated functional groups, they contain a mixture of sp^2- and sp^3- hybridized carbon state which finds multiple potential applications in opto-electronic devices by tuning the relative fraction of sp^2-hybridized domains of GO by reduction chemistry [4].

Currently, much work on photovoltaic application is carried out with high electrical conductive and transparent graphene sheet synthesized by physical synthesis technique. The certain limitations of graphene such as the poor solubility in water/organic solvent and the non-uniform film coating by chemical synthesis techniques established a new dimension to exert effort on the solution processable GO. The as-synthesized GO is an insulator with wide optical bandgap, however the switching in electrical conductivity can be achieved by the controlled deoxidation or partial reduction. In general, large numbers of complicated mechanism are adopted to tailor the electrical property of GO such as high energy irradiation [5], localized and non-localized defects creation [6], introducing large proportion of strong hazardous reducing agents like hydrazine [7] and hydriodic acid [8], surface passivation by anchoring noble metals and metal oxide (Fe [9], Zn [10], Al [11], Sn [12], and SnO_2 [13]), structure directing and chemically filling with metallic element or conducting polymers [14], and many more.

Although with poor electrical conductivity, the GO and the chemically reduced GO still finds an extensive application in the fabrication of photovoltaic device. Li *et. al*. [15] and Murray *et. al*. [16] reported the solution processed reduced graphene oxide (rGO) as an efficient hole transporter in the polymer and organic photovoltaic cell where the efficiency has been improved to 7.5%. An organic photovoltaic device fabricated with an ITO/PEDOT:PSS/P3HT-GO/Al structure rendered an increase in short-circuit current (I_{sc}) and conductivity but a decrease in open circuit potential (V_{oc}) [17]. The rise in the conductivity is evident from the fluorescence and electroluminescence quenching which promotes the easy charge transfer within the device. Similarly, the Cu_2S/rGO sensitized with quantum dot CdSe nanoparticles shows a high fill factor

(*FF*) of ~75% and power conversion efficiency of 4.4% [18]. The rGO/polypyrrole film is fabricated as a counter electrode for dye-sensitized solar cells and shows an improved power conversion efficiency of 8.14% [19]. Marccus *et. al*. demonstrated the presence of GO at the enzyme/electrode interface diminishes the activation energy by decreasing the distance between the electrode surface and the enzyme cofactor thereby, it enable the GO to act as a biofuel cells and biosensors [20]. Even though, with great achievements and introducing new concepts in the photovoltaic device modeling, the photovoltaic cell still lags in tuning high I_{sc} and V_{oc} simultaneously and the stability of the material is uncertain. To overcome the cited constraints such as poor conductivity in GO and an efficient photovoltaic device modeling, an approach is established to design a *pn* hetero-junction based solar cell with Quantum confined CdS functionalizing the GO surface.

Many research articles published on GO/CdS nanocomposites are synthesized by utilizing an external driving force such as autoclave mediated solvothermal process and the usage of specific solvent medium (ethylene glycol) to enrich the homogeneous distribution of CdS nanoparticles on the surface of graphene [21, 22]. Moreover, the as-synthesized GO/CdS nanocomposites are effectively utilized as the fast photocatalyst where the environmental pollutant and waste material degradation are performed [23-25]. In general, the graphene/semiconductor nanocomposites are recognized as active photocatalyst because the addition of semiconductor nanoparticles on graphene surface prevent the aggregation of graphene layers which in turn increases the surface area for the removal of organic pollutants from the aqueous solution [26]. Peng Gao *et. al*. reported that the GO/CdS/Pt composite containing 0.5 at% of Pt exhibits the highest hydrogen evolution rate of 123 $mLh^{-1}g^{-1}$ with strong photostability, which is about 2.5 times higher than that of GO/CdS composite and 10.3 times higher than that of pure CdS [27]. To have a new insight, a simple chemical precipitation method is adopted towards the synthesis of GO/CdS nanocomposites and the same is implemented in the fabrication of hetero-junction based solar cell devices for the first time. Hence, the paper reports the dual performance of quantum confined CdS in enhancing the electrical conductivity of GO and further, improving the power conversion efficiency of *pn* hetero-junction based solar cells.

Here, a simple surface functionalization of GO is employed where the relative composition of oxygen to carbon atom is tuned to improve the electrical conductivity and for the

same, the nanocrystalline CdS is selected to functionalize the GO surface. The optimum optical bandgap of 2.42 eV at 300 K, high absorption coefficient $>10^4$, and *n*-type electrical conductivity enable the CdS to extend the photon absorption over a wide spectral range of the solar spectrum (from visible to UV) and to act as a buffer layer and window absorber in the hetero-junction based solar cell [28, 29]. In addition, the oxygenated functional groups present in the GO surface easily bridge and link the CdS nanoparticles and render a stable chemical structure even at room temperature. Thus, the above features make CdS a promising semiconductor material for photovoltaic cells and open a framework to meet the global energy crisis.

Experimental details

All the chemicals used in the experimental synthesis were of reagent grade and were used without further purification.

Synthesis of GO

The synthesis of GO was followed from the usual modified Hummer's method [30]. Here, the natural graphite flakes were oxidized by the strong oxidizing agents like concentrated sulphuric acid and potassium permanganate. In brief, 2 g of graphite flakes was added to 100 mL of sulfuric acid (H_2SO_4) under constant stirring and the temperature was maintained below 10 °C. Then 8 g of oxidizing agent potassium permanganate ($KMnO_4$) was gradually added to the reactant mixture at the same temperature. The solution mixture was maintained at low temperature and stirred continuously for 2 h. The mixture was cooled in a low temperature bath and subsequently diluted with 100 mL of distilled water. The hydrogen peroxide (H_2O_2, 30% in 20 mL of distilled water) was added to the mixture to dissolve the residual permanganate. A large amount of bubbles were released and the color of the mixture changed to brilliant yellow. The colored suspension was filtered and washed several times with 1 M hydrochloric acid (HCl) and distilled water, thereby to lower the pH. The final residue was mixed with the small proportion of ethanol and poured in the petri dish and dried in hot air oven at 50 °C overnight. The GO sheet was formed and stored in a vacuum dessicator.

Synthesis of CdS nanoparticles

Simple chemical precipitation technique was adopted to synthesize CdS nanoparticles. Here, the cadmium nitrate and thiourea were used as the precursors. In the typical synthesis procedure, 1 mmol of cadmium nitrate and 3 mmol of thiourea were separately dissolved in 27 mL of

ethylene diamine and 23 mL of double distilled water. Further, the cadmium (Cd^{2+}) source and sulphur (S^{2-}) source were mixed together and loaded in 100 mL beaker. The reaction mixture was heated to 180 °C for 8 h and then cooled to room temperature. The yellow product was separated by centrifugation and washed repeatedly with distilled water and ethanol. Finally, the product was air dried and grinded to fine powder.

Synthesis of GO/CdS nanocomposites

The GO/CdS nanocomposite was synthesized by chemical precipitation method. Initially, an optimized amount of GO was dispersed by ultrasonication in 80 mL of double distilled water for 1 h at room temperature. Then, the cadmium nitrate (5 mM) and thiourea (5 mM) were added separately to the GO dispersion with constant stirring. This promotes the good solubility and dispersion of Cd^{2+} ions and S^{2-} ions throughout the GO surface. The sample solution was precipitated by the addition of ammonia solution until the pH of the solution was adjusted to 9. The reactant solution mixture was stirred continuously for 5 h at 60 °C, meanwhile, the color of the solution turned from greenish yellow to black. The color variation and the photographs of GO and GO/CdS dispersion in double distilled water were shown in Scheme 1. The sample powder was centrifuged, dried, and collected for further characterizations.

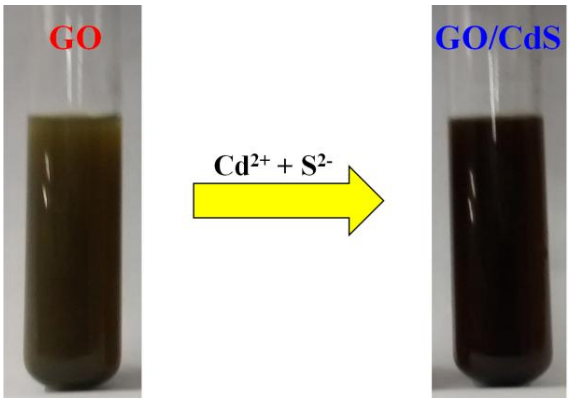

Scheme 1 Photographic view of GO and GO/CdS dispersion

To show the significance of the above synthesis method, the as-synthesized GO and CdS nanoparticles of equal weight ratio were blended together and the corresponding XRD and SEM micrographs were shown in Fig. S1. The CdS nanoparticles were deposited and highly agglomerated on the surface of GO sheet rendering a random distribution. Due to the poor adherence, irregular dispersion and presence of large impurities as observed from the XRD pattern, the CdS blended GO nanocomposites was not considered for further property study.

Device architecture of hetero-junction solar cell

The sol-gel processed spin coating and successive ionic layer adsorption and reaction (SILAR) method were adopted for the film growth. Prior to the film coating, the ITO coated glass substrate was made hydrophilic by immersing in a mild 'basic piranha' solution and cleaned sequentially by sonication in soap solution, distilled water, and a solution of acetone and ethanol (1:1). The cleaned substrates were pre-heated at 400 °C and stored in vacuum dessicator to prevent from contamination.

To evaluate the role of nano CdS, three different combinations of hetero-junction based solar cell was designed. The first device designated as CFG (CdS functionalized GO) was composed of GO/CdS nanocomposites as *n*-type layer and RB as *p*-type layer. Both the layers were successively spin coated on the ITO coated glass substrate. The *n*-type layer was spin coated by dissolving 10 mg of GO/CdS nanocomposites in 10 mL of double distilled water and few drops of ethanol and citric acid were added to stabilize the coating solution. For hetero-junction, the *p*-type layer was achieved by dissolving 1 mg of RB in 10 mL of chloroform. The molecular structure, molecular formula, and the chemical name of RB [31, 32] were represented in the Scheme 2. The characteristic optical absorbance of RB peaked at 552 nm and 559 nm was shown in the Fig. S2.

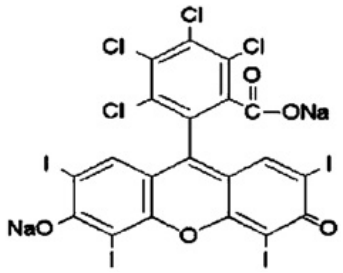

$C_{20}H_4Cl_4I_4O_5$ = tetra-chloro dihydroxy tetra-iodo fluorescein

Scheme 2 Molecular structure and molecular formula of the RB dye

The second and third hetero-junction solar cells fabricated were designated as CSG1 (CdS sensitized GO 1) and CSG2 respectively. In CSG1, the CdS sensitizer acting as a buffer layer was deposited on the ITO electrode by SILAR technique using an ethanolic solution of cadmium nitrate and methanolic solution of thiourea. The buffer layer was successively spin coated by the GO layer and RB layer. Once after the layer-wise deposition of *n*-type and *p*-type material, the film was annealed at 200 °C for 40 min in temperature furnace under air atmospheric condition. The annealing temperature was ascertained from the heat transfer mechanism (ref. Fig. 2(b))

revealing that the -S^{2-} ions present in the GO matrix was retained and not transformed to its oxide form. Similarly, in CSG2, the CdS buffer layer and GO layer were deposited by interchanging the sequence of coating order. Finally, a proper ohmic contact was established on the *n*-type material and *p*-type material by the selective etching of ITO substrate and DC sputtering of Au electrode respectively. The schematic model of photovoltaic device architecture was illustrated in Scheme 3. The cross-sectional images and the approximate thickness were shown in the Fig. S3. As the film layers were coated chemically, the individual layer was not distinguished clearly and the overall thickness was maintained in the range of 105 μm to 120 μm.

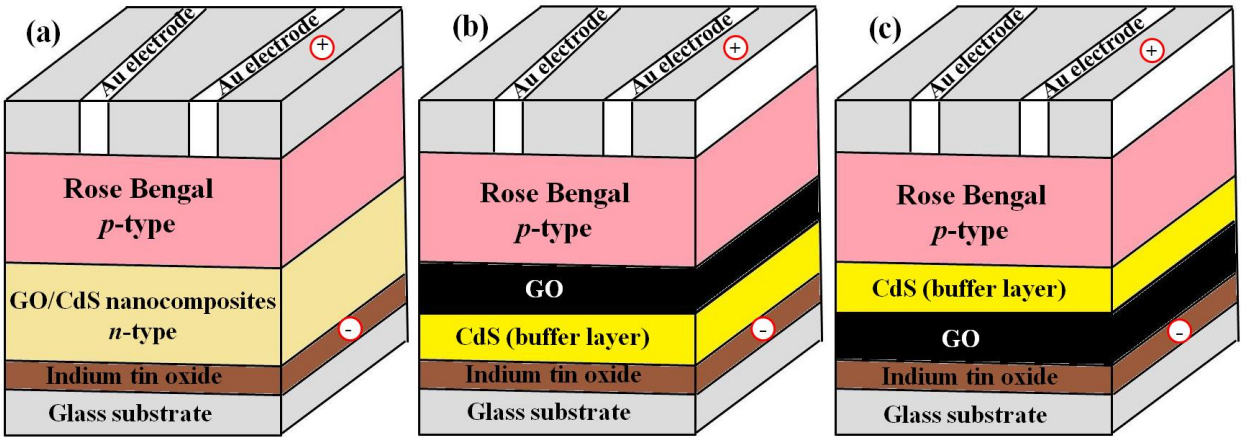

Scheme 3 Schematic models of photovoltaic devices composed of (a) CFG, (b) CSG1, and (c) CSG2

Instrumentation

The structure and the phase purity of GO, CdS nanoparticles and GO/CdS nanocomposite were examined by X-ray diffraction (XRD) measurements, which were performed on Mini Flex IIC with Cu K_α source (λ = 1.5406 Å, 40 kV, 40 mA) and a step size of 0.02° in θ-2θ configuration. The thermal behaviour was analyzed by EXSTAR TG/DTA 6300 at a heating rate of 10 °C/min from room temperature to 800 °C under nitrogen inert atmosphere. The functional group analysis and the nanocomposite formation were confirmed from Fourier transform infrared spectroscopy (FTIR) carried out with FT-IR Perkin Elmer spectrum 2000 spectrophotometer using a potassium bromide pellet technique and Raman analysis was performed with JASCO NRS-300 laser Raman spectrophotometer. The surface morphology and microstructure analysis were carried out using scanning electron microscopy (SEM) measurement on Tescan Vega3 SBU and tunneling electron microscopy (TEM) measurement on Tecnai T30 G^2 S-TWIN. UV-Vis diffuse reflectance spectroscopy (DRS) measurement was acquired using Perkin Elmer

Lambda 650 spectrophotometer in diffuse reflectance mode and the spectra were recorded at room temperature in the wavelength range of 450 nm - 800 nm. The room temperature emission spectra were recorded using Shimadzu (RF-5301 PC) spectrofluorophotometer under an excitation wavelength of 350 nm using a 150 W Xenon lamp. The electrical study was performed with cyclic voltammetry (CV) using Biologic Instrument under varying scan rate and room temperature impedance measurement by Solatron 1260 equipped with dielectric interface analyzer. The current density−voltage ($J-V$) measurements for the device were recorded using a Keithley sourcemeter with 100 mW/cm^2 AM 1.5G of solar spectrum illumination.

Results and discussion

Phase confirmation

The Fig. 1(a) shows the XRD pattern of GO sheet, CdS nanoparticles, and GO/CdS nanocomposites recorded in the range of 2θ = 5° - 80°. The as-synthesized GO exhibited a strong reflection peak at 2θ = 9.797° corresponding to the (002) plane as depicted in Fig. 1(a). From the Bragg's diffraction equation $2dsin\theta = n\lambda$, the interplanar spacing was calculated and found to be 9.0213 Å. The d value of GO is greater than that of pure graphite because of the presence of large number of oxide functional groups and intercalated water (H_2O) molecules [33]. Moreover, once oxidized with the graphite flakes, the (002) peak shifted from higher scattering angle 2θ = 26.6° to 2θ = 9.797° with increased interplanar spacing. In addition to the presence of GO diffraction peak, the traces of starting materials (graphite flakes) were also observed at 2θ = 26.54° and 2θ = 42.32° corresponding to the (002) and (001) plane of graphite (JCPDS data card no. 89-8487) respectively. The appearance of the peaks implies that the GO was not oxidized completely.

The XRD pattern of CdS nanoparticles synthesized by the chemical precipitation technique was represented in Fig. 1(a). The peaks were indexed and compared with the standard JCPDS data card no. 80-0006. The as-synthesized CdS nanoparticles exhibited hexagonal phase crystal structure with the lattice parameter a = 4.121 Å, $b = c$ = 6.682 Å. The high intense reflection peak was observed at 2θ = 26.62° corresponding to the hexagonal (002) plane. The other peaks were indexed at 2θ = 25.06°, 28.24°, 36.82°, 43.94°, 48.06°, 52.16°, 67.19°, 71.26°, 75.97° and the planes were marked as (100), (101), (102), (110), (103), (112), (203), (211) and (105) respectively. The average crystallite size was estimated from the well-known Scherrer formula

d_{avg} = ($0.9\lambda/\beta cos\theta$). The d_{avg} corresponding to the (002) plane of CdS nanoparticles was calculated and found to be 130 nm.

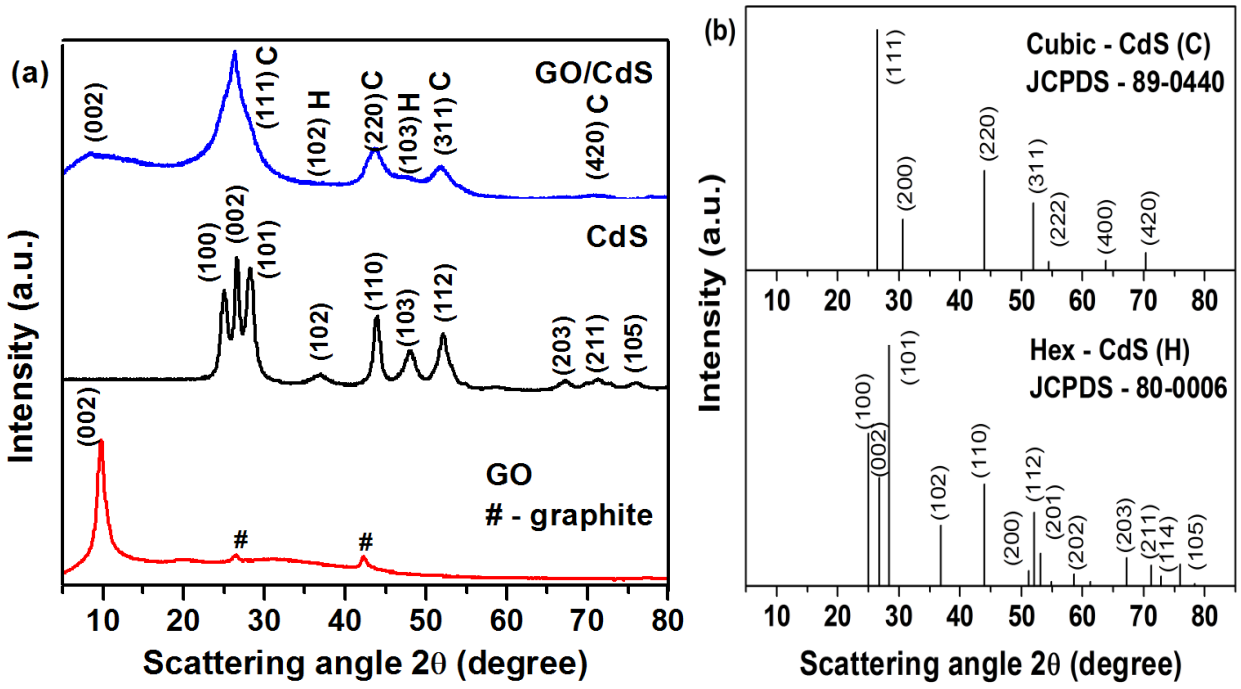

Fig. 1 (a) The XRD pattern of GO sheet, CdS nanoparticles and GO/CdS nanocomposites and (b) Standard JCPDS data for cubic (C) and hexagonal phase (H) CdS

The crystallinity of the GO/CdS nanocomposites was displayed in Fig. 1(a). As the CdS nanoparticles were incorporated into the GO matrix, the diffraction pattern was modified with few observations. Firstly, the strong reflection peak of GO at 2θ = 9.797° was shifted to lower scattering angle of 2θ = 8.54° and the peak was broadened with the full width half-maximum (FWHM) of 18.39°. The shift towards the lower angle implies that the interlayer spacing *d* was further increased to 12.6125 Å due to the inclusion of CdS nanoparticles. Moreover, the *d* value corresponding to the (002) plane of CdS nanoparticles was 3.3472 Å and for the (111) plane of GO/CdS nanocomposites the value was calculated to be 3.3895 Å. The difference arises due to the van der Waals force of interaction acting between the CdS nanoparticles and the GO sheet resulting in the GO sheet separation. The second observation in the XRD pattern of GO/CdS nanocomposite was that the reflection peaks corresponding to the CdS nanocrystal have undergone an incomplete phase transformation. The XRD pattern exhibits a mixed hexagonal phase and cubic phase of CdS nanocrystals as inferred and compared with the standard JCPDS data represented in Fig. 1(b). The peaks corresponding to the hexagonal phase and the cubic

phase were denoted by the letter 'H' and 'C' respectively. The intensity of the 'H' peaks was weak and less pronounced than the 'C' peaks implying, under the given synthesis condition, the as-grown CdS particles with cubic phase were about to transform to stable hexagonal phase. Moreover, the d_{avg} corresponding to (111) plane of cubic CdS nanocrystal was 6 nm and was equivalent to the Bohr exciton radius of CdS. The reduced crystallite size and the presence of mixed phase imply the incomplete nucleation of cubic CdS crystals to stable hexagonal phase. Thus, the assigned synthesis reaction condition was insufficient to fasten the nucleation and the growth rate in GO/CdS nanocomposites. Finally, the nature of GO in GO/CdS nanocomposites can be revealed from the XRD study. The diffraction peak corresponding to the GO was still observed in the XRD pattern of GO/CdS nanocomposites implying that the GO was in the oxidized state. However, the intensity of the diffraction peak was reduced revealing that the GO was partially reduced as large number of oxygenated functional groups was substituted by the CdS nanoparticles. Thus, the XRD result clearly suggests that the CdS nanoparticles were incorporated and resulted in the formation of GO/CdS nanocomposites. The reaction mechanism was further supported from the TG/DTG study and the nature of GO can be inferred from the FTIR study and Raman analysis. The various parameters calculated from the XRD pattern of GO sheet, CdS nanoparticles, and GO/CdS nanocomposites were tabulated in Table 1.

Table 1 Geometric parameters of GO sheet, CdS nanoparticles and GO/CdS nanocomposites

Sample name	**Average crystallite size d_{avg} (nm)**	**Intense peak position (°)**	**FWHM β (°)**	**Interplanar spacing d (Å)**
GO	7	9.797°	1.225	9.0213
CdS	130	26.61°	0.658	3.3472
GO/CdS	GO 0.70	8.54°	18.391	12.6125
	CdS 6	26.38°	3.917	3.3895

Heat transfer mechanism

The thermal stability and the composition of GO, CdS nanoparticles and GO/CdS nanocomposites were analyzed by TG/DTG under nitrogen inert atmosphere at the heating rate of 10 °C/min and the results were displayed in Fig. 2(a-c). In Fig. 2(a), a major weight loss of 21% between 150 °C and 300 °C was ascribed to the removal of CO, CO_2, and the steam from the liable functional groups present in the as-synthesized GO sheet [34]. The similar weight loss

degradation of 10% was also resulted in the formation of GO/CdS nanocomposites as inferred from the Fig. 2(c). The minor weight loss seen below 100 °C in Fig. 2(a) was due to the evaporation of absorbed water molecule intercalated in the as-synthesized GO sheet. Between 300 °C and 800 °C there was a gradual weight loss corresponding to the removal of stable oxygen functional groups adhered to the 2D graphite structures.

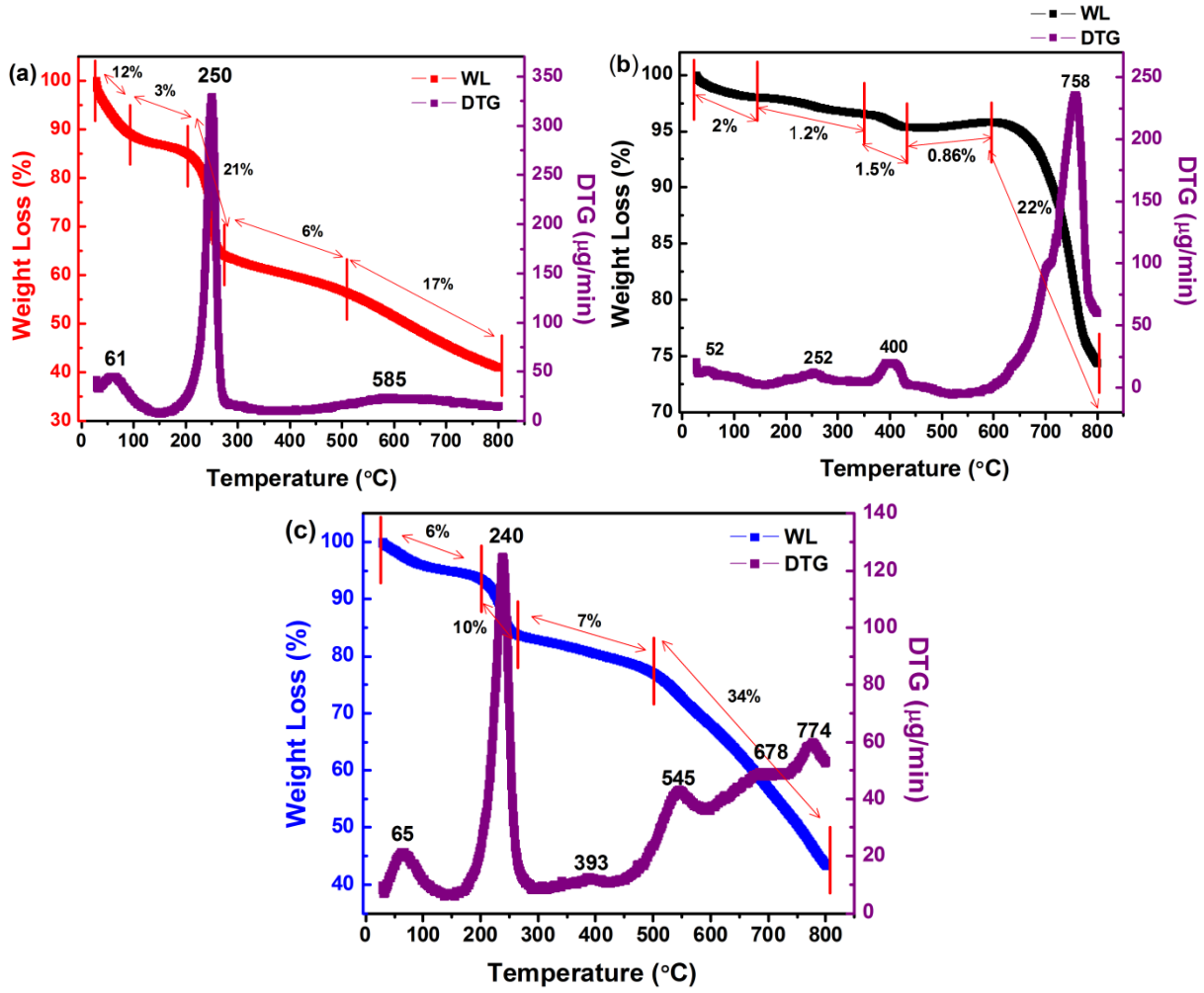

Fig. 2 TG/DTG plot of (a) GO sheet, (b) CdS nanoparticles and (c) GO/CdS nanocomposites

The thermal behavior of CdS semiconductor nanoparticles was shown in Fig. 2(b). A gradual weight loss was observed in the as-synthesized CdS nanoparticles ranging from the room temperature to 600 °C and a sharp weight loss of about 22% was observed between 600 °C to 800 °C. The initial weight loss below 200 °C was attributed to the evaporation of physically absorbed water molecule and molecules with lower molecular mass. The second weight loss between 200 °C and 300 °C was the decomposition of S^{2-} ions hence, the reaction temperature

for the synthesis of CdS nanoparticles was fixed below 300 °C. The remaining change in the weight loss was attributed to the removal of SO_4^{2-} group and NO_3^{2-} group and the adhesion of O^{2-} ions to the Cd^{2+} to form stable CdO material compound. When CdS was incorporated to the GO matrix to form GO/CdS nanocomposites, the same decomposition arises with the slight shift in the peak position as shown in Fig. 2(c). The weight loss appearing at 65 °C, 240 °C, 545 °C follows from the TG analysis of GO (Fig. 2(a)) and the loss at 393 °C, 678 °C, and 774 °C pursued from the CdS nanoparticles (Fig. 2(b)). In GO/CdS nanocomposite, the peak at 545 °C has high relative rate of weight loss in comparison to the GO peak at 585 °C implying the large fraction of oxygen removal from the GO surface due to the inclusion of CdS nanoparticles. This clearly suggests the formation of GO/CdS nanocomposites and the GO has undergone a partial redox reaction for the nucleation of CdS nanoparticles.

Functional group analysis

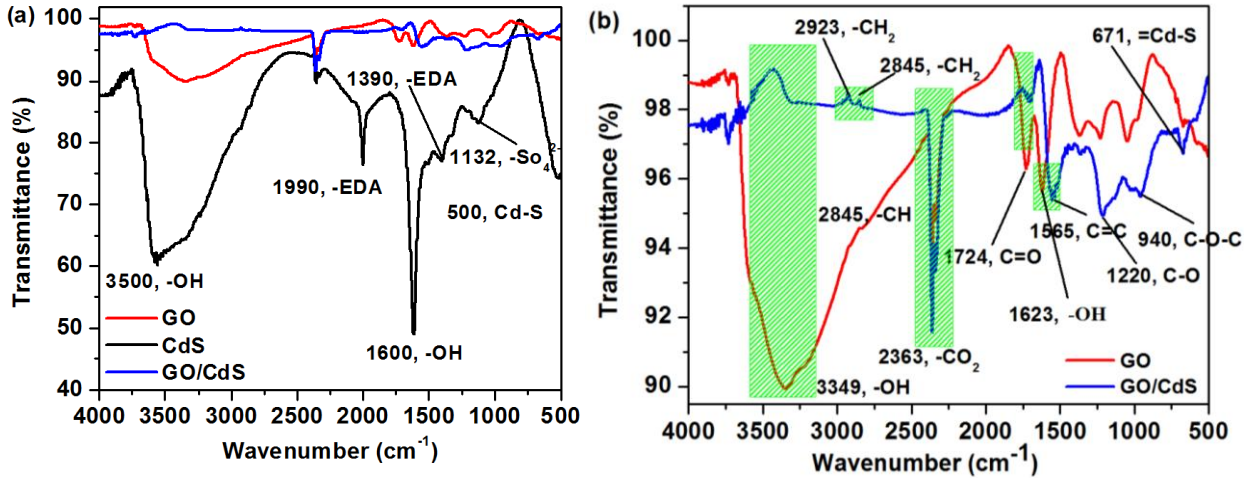

Fig. 3 (a) FTIR transmittance spectra of GO sheet, CdS nanoparticles and GO/CdS nanocomposites and (b) an enlarged view of the transmittance spectra obtained for GO sheet and GO/CdS nanocomposites

To confirm the formation of GO/CdS nanocomposites and to ascertain the nature of interaction between the GO sheet and CdS nanoparticles, the FTIR study and Raman study were performed. The FTIR spectra show a wide variation in the transmittance intensity. The transmittance spectrum of CdS nanoparticles shown in Fig. 3(a) comprises of -OH stretching and bending vibration of water molecules at 3500 cm^{-1} and 1600 cm^{-1}, C=S stretching vibration of thiourea at 650 cm^{-1}, the SO_4^{2-} functional group at 1132 cm^{-1}, and band at 506 cm^{-1} corresponds to the Cd-S stretching frequency [35]. The vibrational frequency observed around 1390 cm^{-1} and

1990 cm^{-1} were related to the solvent medium ethylene diamine adsorbed on the surface of the CdS nanoparticles.

To define the characteristic adsorption peaks in GO and GO/CdS nanocomposites an enlarged view of FTIR spectra were shown in Fig. 3(b). The characteristic functional groups of GO were located at 3349 cm^{-1}, 1724 cm^{-1}, 1565 cm^{-1}, and 1220 cm^{-1} and were assigned to the OH stretching of intercalated water molecule, C=O stretching of COOH group, C=C stretching vibration of alkyne, and C-O stretching vibration respectively. In comparison, the above assigned peaks were observed in the GO/CdS nanocomposites but, with reduced intensity or almost disappeared indicating that the oxygenated functional groups in GO were reduced partially. Moreover, the inclusion of CdS nanoparticles was confirmed from the presence of the characteristic Cd-S stretching vibrational peak at 671 cm^{-1} which was red shifted in comparison to the peak in pure CdS nanoparticles. Thus, the FTIR spectra conclude that the atomic composition of oxygen in GO/CdS nanocomposites was less than that in GO and the CdS nanoparticles were included in the GO matrix. The large variation in the transmittance intensity for GO and GO/CdS nanocomposites were highlighted in the Fig. 3(b).

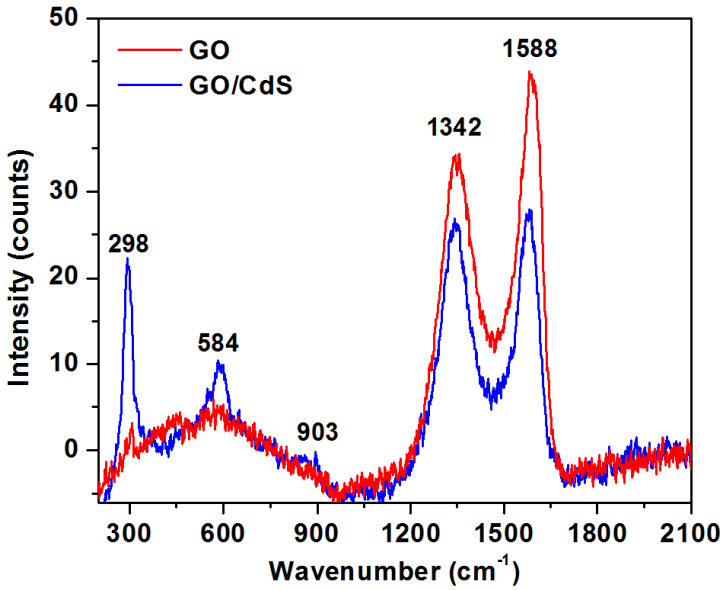

Fig. 4 Raman spectrum from (a) GO and (b) GO/CdS nanocomposites

The Fig. 4 represents the Raman scattering measured on GO and GO/CdS nanocomposites in the wavenumber ranging from 250 cm^{-1} to 2100 cm^{-1}. The Raman spectrum of GO consists of two sharp peaks at 1342 cm^{-1} and 1588 cm^{-1} corresponding to the *D*-band and *G*-band of GO respectively. The intensity of the *D* band (I_D) was related to the presence of defects and disorders

of surface modified GO sheet and the I_G band was associated with the vibration of sp^2-hybridized carbon atoms in 2D hexagonal lattice of GO [36]. The similar peaks appear for GO/CdS nanocomposites but, with the reduced intensity. The relative intensity ratio of *D*-band to *G*-band of GO and GO/CdS nanocomposites was 0.76 and 0.94 respectively. The enhancement in the relative intensity ratio I_D/I_G of GO/CdS nanocomposites reflects the relative fraction of sp^2-hybridized carbon atom was lowered and the distorted structure of GO/CdS nanocomposites due to the redox reaction for the nucleation of CdS nanoparticles on the surface of GO. In addition to the *D*-band and *G*-band peaks, three optical vibrational Raman active modes of CdS nanoparticles were observed. The peaks at 298 cm^{-1}, 584 cm^{-1} and 903 cm^{-1} were assigned to the fundamental longitudinal optical phonon mode 1LO, the first overtone mode 2LO, and the second overtone mode 3LO of CdS nanoparticles respectively [37]. The presence of the above peaks gives an evident for the inclusion of CdS nanoparticles to GO.

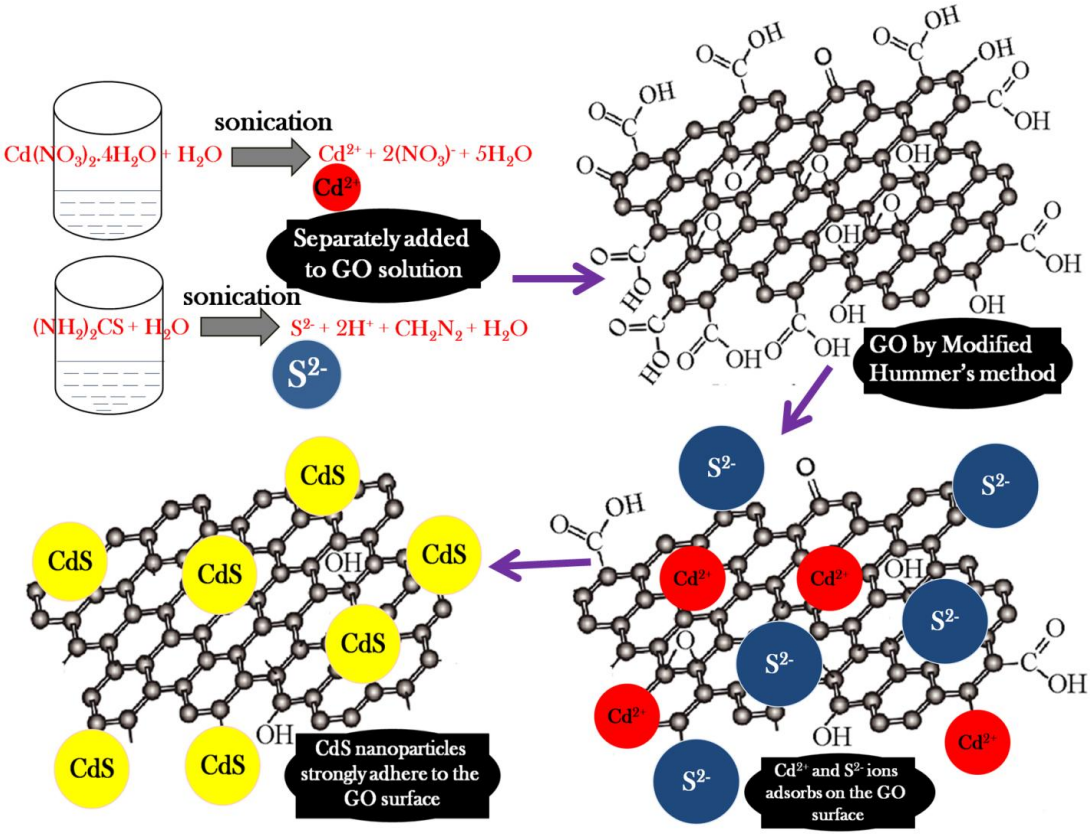

Scheme 4 Possible reaction mechanism inferred in CdS functionalized GO nanocomposites

From the heat transfer mechanism, FTIR study and Raman analysis, the probable redox reaction and the nature of interaction between the GO sheet and CdS nanoparticles was ascertained and illustrated in the Scheme 4. The cadmium nitrate and thiourea solution were

sonicated individually for 1 h so as to detach the Cd^{2+} ions and S^{2-} ions from the respective chemical precursor. The slow addition of Cd^{2+} ions and S^{2-} ions to the dispersed GO solution render an easy solubility, uniform dispersion, and maximum substitution of the ions to the oxygenated functional groups adhered to the GO surface. The suitable reaction condition and the strong affinity favors the adsorbed ions to form CdS nanoparticles on the surface of GO.

Morphology study

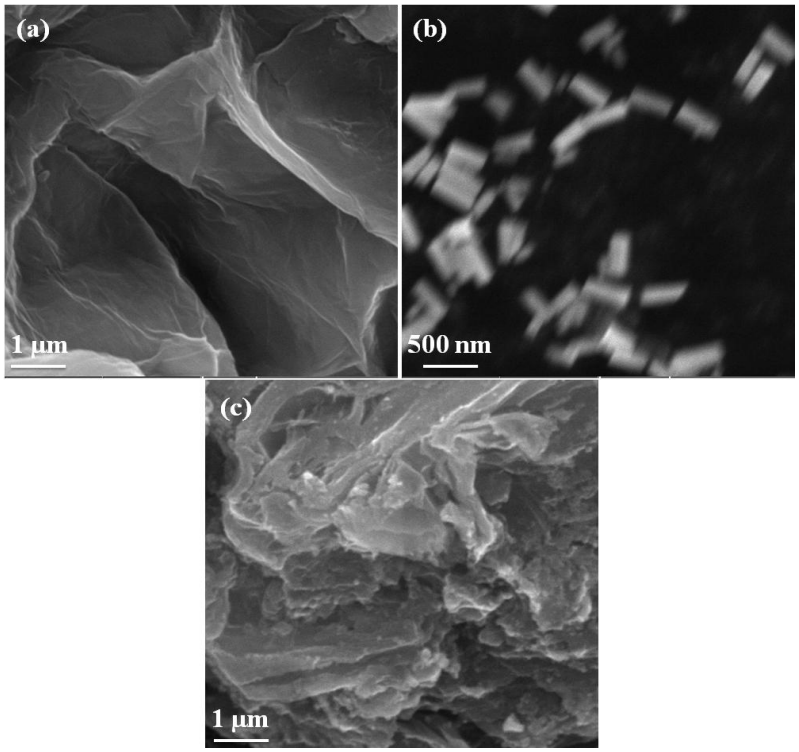

Fig. 5 The SEM micrographs of (a) GO sheet, (b) CdS nanorods and (c) GO/CdS nanocomposites

The Fig. 5(a-c) shows the SEM images of the GO sheet, CdS nanorods, and CdS incorporated GO sheet dried under air atmosphere. The GO exhibits 2D sheet like morphology with highly wrinkled surface and the edges represent many numbers of folds with high degree of curvature. Due to the presence of folds and curvature, the number of GO layers and the boundaries between the sheets were unable to be distinguished in the chemically as-synthesized GO. However, when CdS nanoparticles were dispersed in the GO, the surface of the GO sheet becomes rough, highly curled and densely packed with spherically shaped CdS particles. A close observation of the SEM image displayed in Fig. 5(c) reveal that the CdS nanoparticles were homogeneously distributed and enwrapped in the GO. The even distribution of CdS

nanoparticles on the 2D GO and the intimate interaction between them exerts a profound influence on the hybrid material properties. However, the blended compositions of CdS nanoparticles on GO render a random distribution with aggregation and agglomeration as shown in Fig. S1. Moreover, the SEM image in Fig. 5(b) reveals that the pure CdS nanoparticles synthesized by chemical precipitation method were rod shaped with average length of 340 nm and width of 120 nm. The amine group along with water molecule present in the reactant medium have served as structure directing agent and thus, promoting 1D growth [38]. The rods were dispersed individually and exhibited narrow particle size distribution.

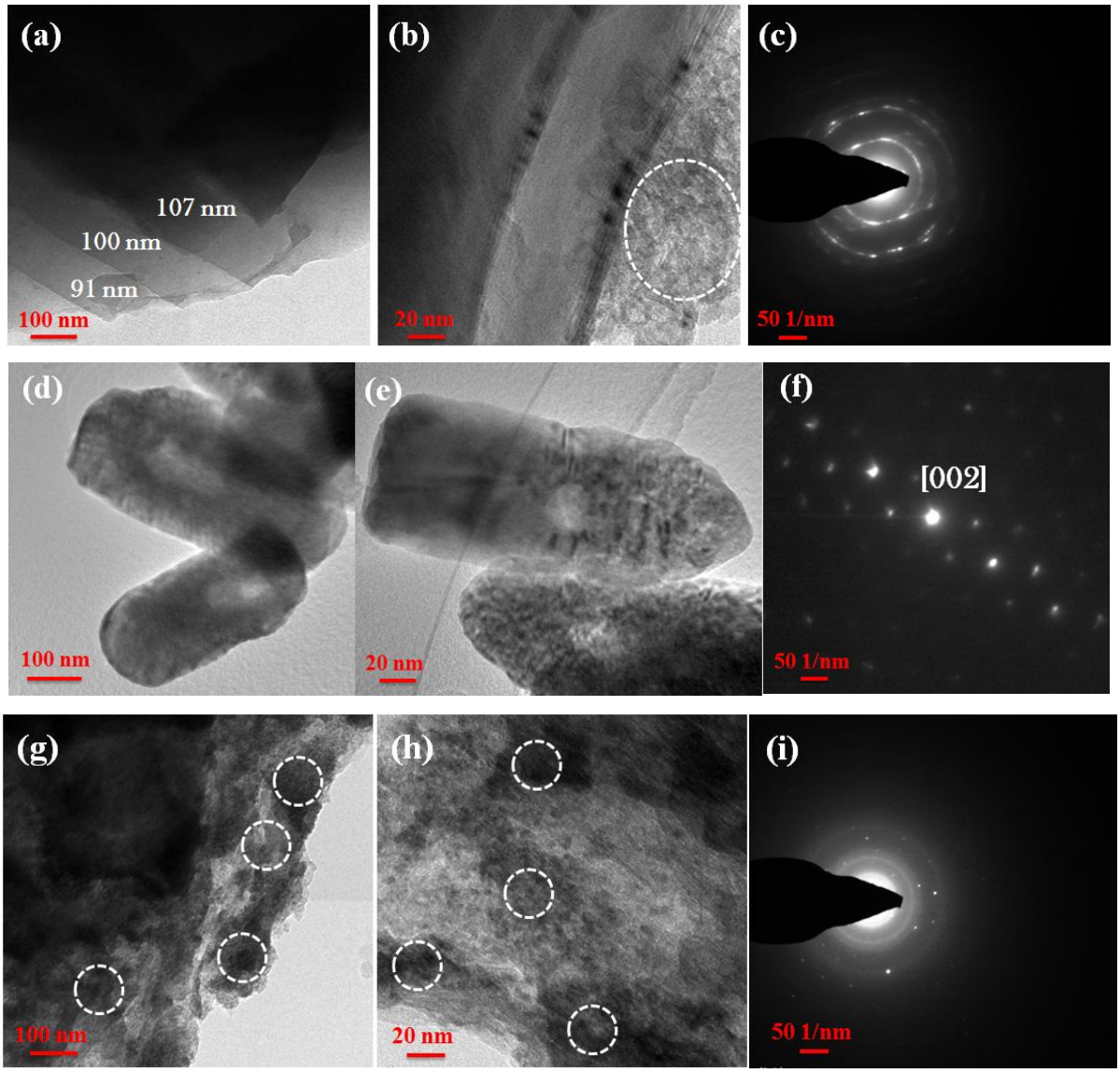

Fig. 6 TEM and SAED pattern of (a-c) GO sheet, (d-f) CdS nanorods and (g-i) GO/CdS nanocomposites

The surface morphology of the as-synthesized samples was further examined by TEM. The multilayered 2D GO structures with nearly regular spacing (100 ± 9 nm) were clearly seen in Fig. 6(a). In high magnified TEM image displayed in Fig. 6(b), the oxygen functional group (denoted by dotted circle) adhered to the edge plane of graphite was noticeable which enable the GO to be stacked one over the other. Thus, the as-synthesized GO was in oxidized state as evident from the TEM micrographs. The selected area electron diffraction (SAED) pattern shown in Fig. 6(c) displays a ring pattern and the regular spacing in the GO layer was highly reflected. The CdS nanoparticles synthesized from the cadmium nitrate and thiourea precursors were rod shaped and the length of the rods were in the range of 220 nm to 370 nm and the width in the range of 90 nm to 110 nm (refer Fig. 6(d-e)). The SAED pattern represented in Fig. 6(f) was hexagonal dot pattern implying the 1D oriented growth of CdS nanoparticles along [002] direction as confirmed from the XRD study. The TEM images of GO/CdS nanocomposites were portrayed in Fig. 6(g-h). Here, the CdS nanoparticles were highly dispersed in the GO matrix and such distribution renders best material properties in hybrid hetero-structures. Moreover, the CdS nanoparticles nucleated on the surface of GO were very small in size and denoted by dotted circle. The SAED pattern of GO/CdS nanocomposites was shown in Fig. 6(i). The reflections originating from the GO were amorphous in nature whereas, the dotted reflections were from the CdS nanoparticles. The dotted reflections were random in nature and can be attributed to the presence of the mixed phase (cubic phase ‘C’ and hexagonal phase ‘H’) CdS nanoparticles as estimated from the XRD pattern (ref. Fig. 1(a)).

However, to determine the individual particle size of CdS nanoparticles and to confirm the mixed phase of CdS in GO/CdS nanocomposites, HRTEM images along with the SAED were presented in Fig. 7(a-c). The particles were arranged lamellar-leaf like structure and the individual particle diameter range from 6.20 nm to 7.70 nm. In Fig. 7(b), the lattice spacing was clearly resolved and the *d* spacing was calculated to be 0.3346 nm revealing the cubic phase of CdS nanoparticles. Further, the formation of GO/CdS nanocomposite and the presence of mixed phase in CdS were confirmed from the SAED pattern as shown in Fig. 7(c). The high intense reflection indicated as spot 1 in Fig. 7(c) corresponds to the (002) plane of GO material. The remaining reflections originate from the mixed phase of CdS nanoparticles enwrapped in the GO matrix. In addition, the reflections from the trace material graphite were also observed in the SAED pattern. The *d* spacing values of various phases and the corresponding (hkl) planes were

signified in the Fig. 7(d). Thus, the HRTEM images and SAED pattern of GO/CdS nanocomposites were in good agreement with the XRD pattern.

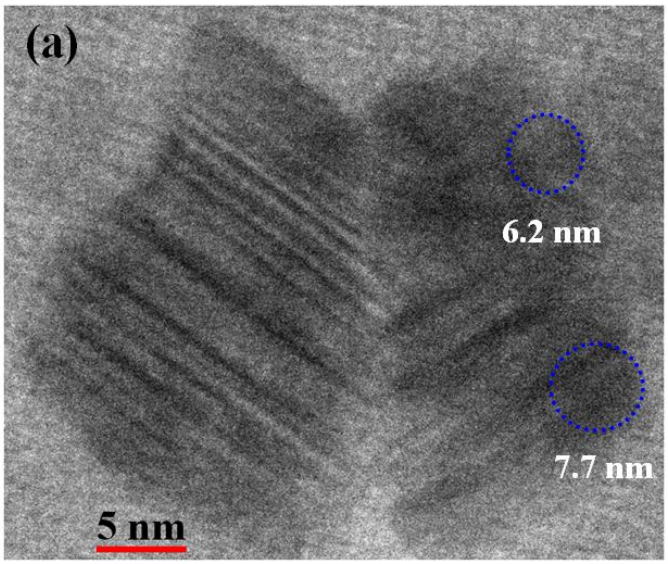

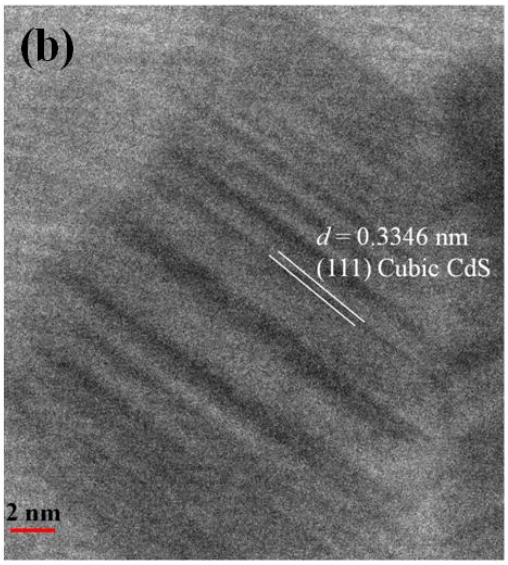

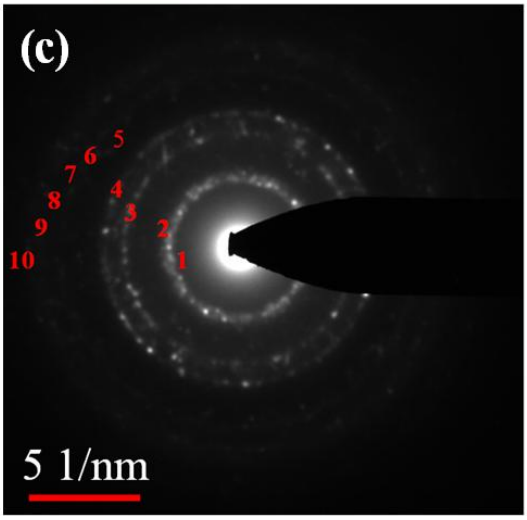

(d)

Spot Position	*d* spacing value (nm)	(hkl) plane	Crystal Structure
1	0.3320	(002)	GO
2	0.3164	(101)	CdS – H
3	0.2370	(102)	CdS – H
4	0.2020	(101)	Graphite
5	0.1881	(102)	Graphite
6	0.1763	(311)	CdS – C
7	0.1460	(400)	CdS – C
8	0.1328	(211)	CdS – H
9	0.1165	(213)	CdS – H
10	0.1123	(511)	CdS – C

Fig. 7 (a-b) HRTEM images, (c) SAED pattern and (d) the corresponding *d* spacing values of GO/CdS nanocomposites

Absorbance and emission study

UV-visible DRS was employed to study the optical absorption of CdS nanoparticles, GO sheet, and GO/CdS nanocomposites. The optical absorption spectra of GO and GO/CdS along with CdS nanoparticles were presented in Fig. 8(a). The optical absorption edge of as-synthesized CdS nanoparticles was found to be around 515 nm and corresponds to the charge transfer from the valence band of S^{2-} ions to the conduction band of Cd^{2+} ions. The GO sheet do not exhibit any absorption in the visible region of the solar spectrum as they act as an insulator.

After the inclusion of CdS nanoparticles, the optical absorption of GO/CdS nanocomposites was drawn to the visible region and the absorption edge was tremendously blue shifted towards the lower wavelength region in comparison to the absorption edge of as-synthesized CdS nanoparticles. The blue shift in the optical absorption can be explained by the quantum confinement or size quantization effect. From the XRD pattern, the average crystallite size of as-synthesized CdS nanoparticles was 130 nm while that of GO/CdS nanocomposites was 6 nm equivalents to the Bohr exciton radius of CdS nanoparticles. The reduced crystallite size, the homogeneous distribution of CdS nanoparticles in the GO matrix and the strong interaction between GO and CdS lead to an obvious blue shift in the absorption peak of GO/CdS nanocomposites. The optical absorption in the visible region was enhanced by the inclusion of Quantum confined CdS nanoparticles into the GO and thus, serves as a promising material in the photovoltaic device applications.

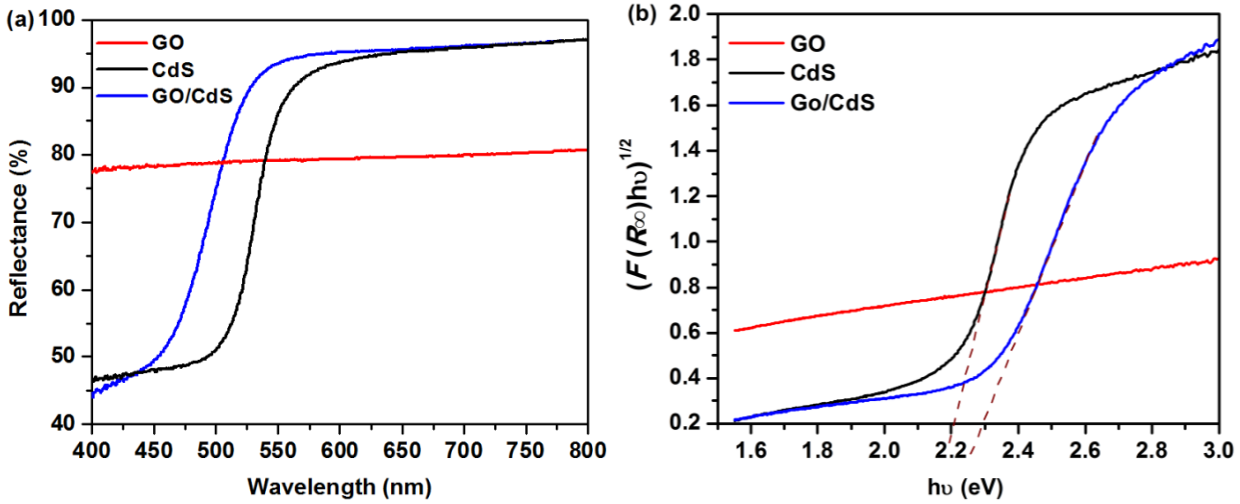

Fig. 8 (a) UV-visible DRS absorption spectra and (b) optical bandgap of GO sheet, CdS nanorods and GO/CdS nanocomposites

Further, the optical bandgap was estimated from the Kubleka-Munk function [39] as shown in Fig. 8(b). The equation was represented as $F(R_\infty) = \frac{(1-R_\infty)^2}{2R_\infty} = \frac{K(\lambda)}{s(\lambda)} \propto \alpha = \frac{(h\upsilon - E_g)^2}{h\upsilon}$ where $F(R_\infty)$ was the K-M function or re-emission function, R_∞ was the diffuse reflectance of an infinitely thick sample, $K(\lambda)$ was the absorption coefficient, $s(\lambda)$ was the scattering coefficient, and $h\upsilon$ was the photon energy. The E_g was determined by extrapolating the linear portion (denoted by dotted line in the Fig. 8(b)) of the plot

obtained between $[(F(R_\infty)hv)^{1/2}]$ versus *hv*. The optical bandgap of as-synthesized CdS nanorods and GO/CdS nanocomposites was 2.2 eV and 2.3 eV respectively.

The Fig. 9 shows the room temperature luminescence emission spectra of GO sheet, CdS nanoparticles and GO/CdS nanocomposites excited at 350 nm and the spectra were recorded in the wavelength of 400 nm to 800 nm. The GO shows flat band with no emission whereas, the CdS nanoparticles show a broad emission covering the maximum visible region of the spectrum (470 nm to 750 nm) with three distinct peaks centered at 540 nm, 570 nm and 650 nm. The near band edge emission peak at 540 nm corresponds to the recombination of free excitons of CdS nanoparticles. The other emission peaks were attributed to the presence of surface defects and vacancies in the as-synthesized CdS nanoparticles. The excess Cd atoms present in the CdS can lead to the formation of an acceptor level within the CdS optical band gap. Thus, the defect band at 570 nm was attributed to the transition of Cd-interstitial donors to the valence band. The shoulder peak at 650 nm was attributed to the recombination of an electron trapped in a sulfur vacancy with a hole in the valence band of CdS [40].

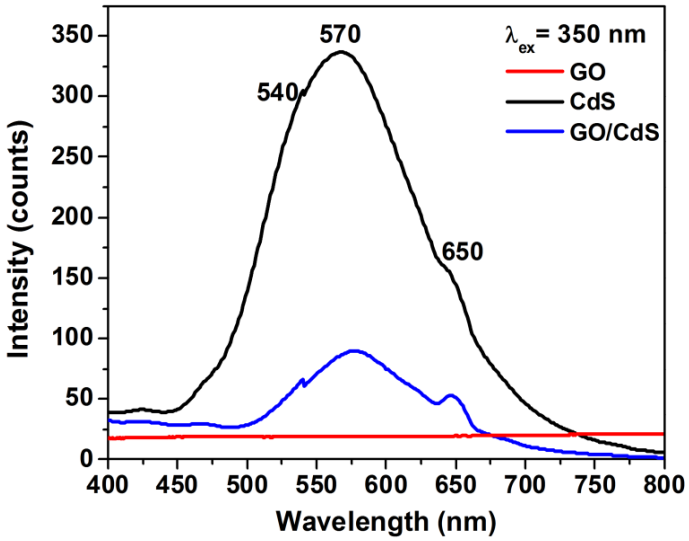

Fig. 9 Room temperature luminescence emission of GO, CdS nanoparticles, and GO/CdS nanocomposites

In the spectrum of GO/CdS nanocomposites, the emission of GO/CdS nanocomposites was almost the same as that of pure CdS nanoparticles. However, there was a slight shift in the peak position and significant fluorescence quenching. The introduction of CdS nanoparticles of reduced crystallite size to the GO surface alters the van der Waals force of interaction between the GO layers and the electrostatic force of interaction between the CdS and GO. The above

interactions result in the variation of the energy levels and hence, shift in the emission peak. The inclusion of CdS nanoparticles exhibit surface related trap centre which acts as a non-radiative electron hole recombination centre or de-excitation centre for the photo-generated charge carriers [41]. Thus, the fluorescence emission quenches, indicating the high surface interaction of CdS to GO sheet and an efficient electron transfer from the CdS nanoparticles to GO. The PL study clearly suggests the choice of CdS nanoparticle inclusion to GO will improve the photovoltaic performance.

Electrical study

CV measurement

The electrode preparation for CV measurement was carried out by mixing 80% of the active material, 10% of the ethanol solvent and 10% of the Nafion binder and this composition was found to be optimal. Then the mixture was dispersed to homogeneous slurry and the slurry was pasted on the surface area of glassy carbon working electrode and dried at 80 ^{o}C in the hot air oven for few minutes. In the preparation of electrolyte, 0.1 M solution of Na_2SO_4 was utilized and the CV curves were recorded in the range of 0.0 V to 0.5 V at different scan rates of 10 mVs^{-1}, 50 mVs^{-1}, and 100 mVs^{-1}.

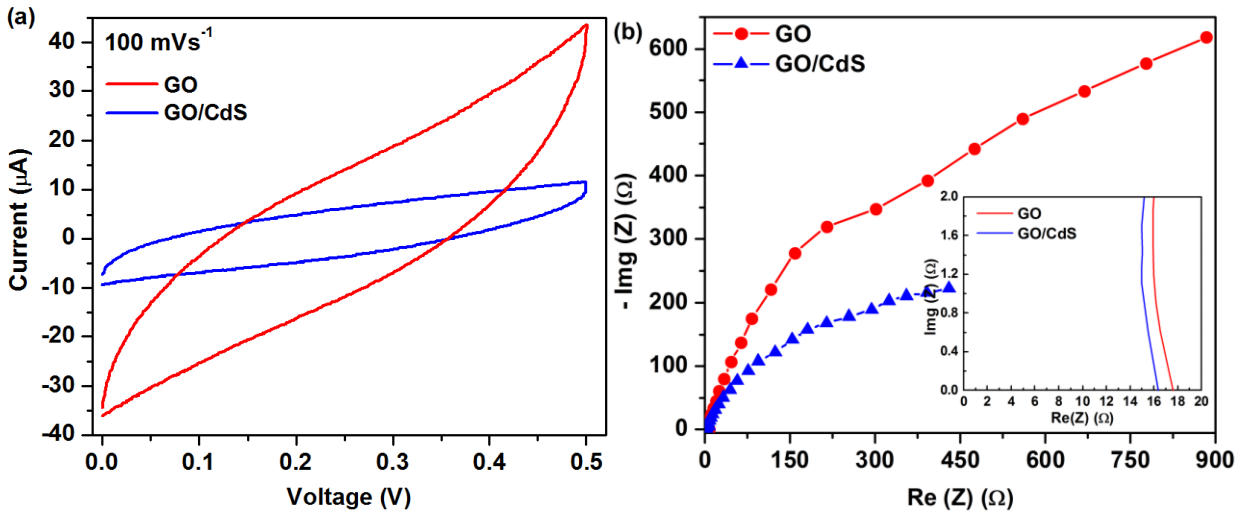

Fig. 10 (a) CV curves for GO sheet and GO/CdS nanocomposites working electrodes in 0.1 M Na_2SO_4 electrolytes tested at a scan rate of 100 mV/s and (b) Nyquist plot for GO sheet and GO/CdS nanocomposites and the inset shows the enlarged view.

The CV curve of GO and GO/CdS nanocomposites recorded at 100 mVs^{-1} scanning rate was displayed in Fig. 10(a). Here, the obtained voltammograms do not exhibit distinct anodic

potential and cathodic potential in the applied potential range of 0.0 V to 0.5 V, implying the participation of capacitive current. From the average integral area of the CV curve, the specific capacitance C_s of the material can be calculated. The mathematical equation of C_s was $C_s = (i)/(r \times m)$ where, i the average current performed over the positive or negative half cycle, m the initial mass loaded to the electrolyte and r the potential sweep rate or scan rate (100 mVs^{-1}). As the capacitance was proportional to the integral area, the GO nanosheet exhibits a higher C_s value of 220 Fg^{-1} while that of GO/CdS nanocomposites was 138 Fg^{-1}. The C_s value of GO nanosheet was nearly 1.6 times greater than GO/CdS nanocomposites implying a higher ion storage capacity in the former. This significant feature was due to the maximum contribution of pseudo-capacitance from the oxygenated functional groups adhered on the surface of GO sheet [42]. The CV curves of GO and GO/CdS nanocomposites at different scan rates (10 mVs^{-1}, 50 mVs^{-1}, and 100 mVs^{-1}) were displayed in the Fig. S4 and their integral area of the curve were improved gradually with the increase in the scan rate.

EIS measurement

The Fig. 10(b) represents the Nyquist plots of GO and GO/CdS nanocomposites. The two impedance curves exhibit semicircle in the high frequency region and the semicircle in GO/CdS was smaller than GO. With the inclusion of CdS nanoparticles, the semicircle of GO/CdS nanocomposites becomes small, indicating a decrease in the interface layer resistance and the charge transfer resistance on the surface. The steep rise in impedance with more vertical nature towards the high frequency region reveals the better capacitive performance in GO than GO/CdS nanocomposites as deduced from the CV characterization. The inset of Fig. 10(b) shows the enlarged Nyquist plot of GO and GO/CdS nanocomposites. The intersection of the curve along X-axis depict the internal resistance or equivalent series resistance (ESR) offered by the material and determined to be 16.20 Ω and 17.80 Ω for GO/CdS and GO respectively. The slightly higher ESR value of GO was probably due to the oxide functional groups residing on the GO surface. In the impedance curve, the semicircle portion observed at the high frequency corresponds to the electron transfer limiting process and can be measured directly from the semicircle diameter. When GO was functionalized with the CdS, the diameter of the semicircular Nyquist plot was reduced dramatically indicating the high accelerating charge transfer. Thus, the low electron transfer resistance (440 Ω) and low internal resistance offered by the GO/CdS nanocomposites reveals the improved electrical conductivity and the facile promotion of charge between the

GO/CdS and the electrode thus, maximizing the charge collection efficiency. Hence, the electrical study using CV and EIS techniques confirms the improved electro-conductivity and fast charge transport process due to the inclusion of CdS nanoparticles. The frequency dependent impedance (Bode plot) for GO and GO/CdS nanocomposites was plotted in Fig. S5 and the plot shows that the impedance gradually fall and attain constant at the high frequency regime.

Photovoltaic measurement

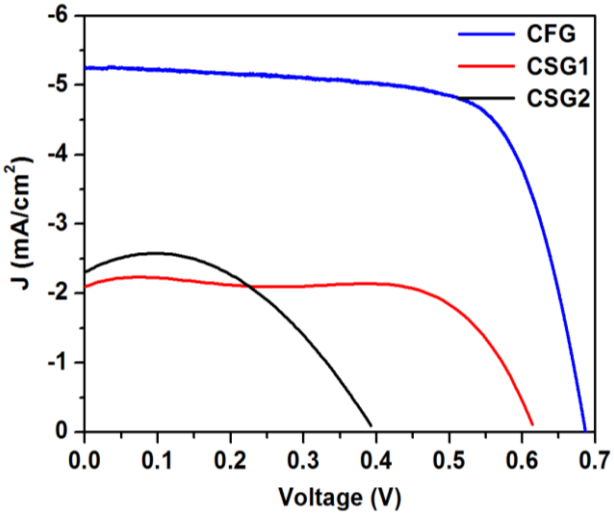

Fig. 11 Current density and voltage characteristics of CdS functionalized GO (CFG) and CdS sensitized GO (CSG) solar cells under AM1.5 (100 mW/cm^2) solar illumination

The photovoltaic cell designing was intended to fulfill the basic requirements like extensive photon absorption, facile charge separation and charge transportation [43]. The Fig. 11 represents the photovoltaic measurement conducted under steady state condition where a constant voltage of 0.0 V to 0.7 V was applied to the devices. The influence of CFG in device performance was evaluated by comparing the *J*–*V* characteristics of CSG. The solar cell parameters of the devices, including the J_{sc}, V_{oc}, *FF*, and η values were tabulated in the Table 2.

Table 2 Photovoltaic performance of CSG and CFG based hetero-junction solar cells

Photovoltaic devices	V_{oc} **(mV)**	J_{sc} **(mA/cm^2)**	***FF*** **(%)**	η **(%)**
ITO/CSG1/RB/Au	615	2.085±0.063	73	0.94±0.028
ITO/CSG2/RB/Au	392	2.418±0.073	66	0.48±0.014
ITO/CFG/RB/Au	685	4.071±0.122	71	1.97±0.059

From the table, it was found that the solar cell with the CFG/RB hetero-junction exhibited higher efficiency of 1.97% than CSG. The V_{oc}, J_{sc}, and *FF* values of CFG were all tuned simultaneously and appreciable in comparison to the earlier reports on hetero-junction based solar cells [17, 18]. In CSG1 and CSG2, the oxygenated functional groups present in GO shields the charge transformation from the CdS nanoparticles (buffer layer) to GO and from the GO to CdS respectively. The hindrance offered in the charge transport results in insignificant η value and the value was lower for CSG2 than CSG1. The causes for such drastic variation were; (i) GO being an insulator with wide optical bandgap, the light trapping in the visible region of the solar spectrum was highly inhibited which in turn reduce the fraction of photo-generated charge carriers and the facile charge transfer from the GO to CdS in comparison to the electron transfer process from the photo-excited CdS quantum dots to the GO matrix, (ii) the deposition of GO between the metal electrode and semiconductor CdS was found to alter the work function of the electrode and decrease the injection of charge carriers into the PV device due to the high degree of oxygenated functional groups present on the GO surface and thus, lowers the V_{oc}.

Moreover, to reveal the significance of CdS nanoparticles towards the functionalization of GO, the photovoltaic cell was designed with the CdS/RB *np* hetero-junction and the solar cell performance was evaluated and depicted in the Fig. S6. The efficiency of CdS/RB was found to be 0.41% and the low efficiency clearly reveals that the *n*-type CdS nanoparticles alone cannot promote the easy transport of charge carriers between the hetero-junction and the collecting electrodes. The PL spectrum of CdS nanoparticles (refer Fig. 9) shows the presence of defect bands at 570 nm and 650 nm which were attributed as the electron trap centre and hence, prevent the facile transfer of electrons between the junction and thus, lowers the current density (1.4 mA/cm^2) and solar efficiency.

But, for the photovoltaic device applications, the hetero-junction should promote facile charge transport, which, can be achieved by the complete reduction of GO to graphene. However, the graphene are no longer dispersible in water/organic solvent and the high transparency was lost which were essential for the uniform film coating and for the maximum adsorption of photon energy respectively. Based on the above crisis, the as-synthesized GO was reduced partially by the surface functionalization of CdS nanoparticles and thus, compensating both the characteristics. Thus, in CFG, the sp^2- hybridized structure of GO was destructed by the inclusion of CdS nanoparticles which resides either at the edges or on the surface of GO sheet

and therefore, leads to the formation of defects. The strained region of GO lattice exhibits higher chemical reactivity and consequently easy displacement of electron density from the upper plane of the sheet. This surface alteration and homogeneous distribution of quantum confined CdS nanoparticles on the GO surface render facile and rapid charge (electron and hole) transfer within the device. In addition, the size quantized CdS nanoparticles (d_{avg} = 6 nm) with low optical band gap of 2.3 eV was included to absorb wide range of the solar spectrum and the nanoscale mixing of CdS nanoparticles into the GO matrix increases the interfacial area and produce large number of excitons per incident photon. Further, the fluorescence quenching observed in the PL spectrum and the low interface resistance measured from the EIS facilitates the non-radiative recombination pathway for the electron-hole separation and transportation, thus, simultaneously controlling the J_{sc}, V_{oc}, and η parameters of the CFG photovoltaic device.

Conclusions

In conclusion, we have established a simple solution processable quantum confined CdS inclusion method to enhance the electrical property of GO and to promote the facile charge transport for photovoltaic application. The enhancement was attributed to the maximum light absorption in the visible region of the solar spectrum offered by the low optical bandgap CdS, facile charge transport which arises from the homogeneous distribution of CdS nanoparticles in multilayered GO sheet and reduced contact resistance present at the hetero-junction interface. The CV and EIS studies showed that the GO/CdS has charge storage capability of 138 Fg^{-1} and improved electrical conductivity thus, switching the GO from an insulator to semiconducting nature. Moreover, in comparison to CdS sensitized GO which acts as a separate buffer layer, the CdS functionalized GO exhibited sustainably improved solar cell efficiency of 1.97% and established an overall control over the photovoltaic cell parameters. The present work demonstrates the advantage of nano CdS inclusion in GO for photovoltaic application and possibly the GO/CdS nanocomposites paves the way towards the fast electrocatalytic activity, electrochemical biosensor and high sensitivity gas sensors.

Acknowledgements

We acknowledge University Grant Commission (UGC), New Delhi, India for the financial support *via* the Dr. D. S. Kothari Post-doctoral Fellowship 2012. We owe a deep sense

of gratitude to all the research scholars, Centre for Nanoscience and Technology, Anna University, Chennai for ensuring the facilities and instruments available in the laboratory.

Notes and references

1 K. S. Novoselov, A. K. Geim, S. V. Morozov, D. Jiang, Y. Zhang, S. V. Dubonos, I. V. Grigorieva and A. A. Firsov, Electric field effect in atomically thin carbon films, *Sci.*, 2004, **306**, 666-669

2 D. Chen, H. Feng and J. Li, Graphene oxide: Preparation, functionalization, and electrochemical applications, *Chem. Rev.*, 2012, **112**, 6027-6053

3 Y. Zhu, S. Murali, W. Cai, X. Li, J. W. Suk, J. R. Potts and R. S. Ruoff, Graphene and graphene oxide: Synthesis, properties, and applications, *Adv. Mater.*, 2010, **22**, 3906-3924

4 D. R. Dreyer, S. Park, C. W. Bielawski and R. S. Ruoff, The chemistry of graphene oxide, *Chem. Soc. Rev.*, 2010, **39**, 228-240

5 Y. Tao, B. Varghese, M. Jaiswal, S. Wang, Z. Zhang, B. Oezyilmaz, K. P. Loh, E. S. Tok and C. H. Sow, Localized insulator-conductor transformation of graphene oxide thin films via focused laser beam irradiation, *Appl. Phys.* A, 2012, **106**, 523-531

6 C. G. Navarro, R. T. Weitz, A. M. Bittner, M. Scolari, A. Mews, M. Burghard and K. Kern, Electronic transport properties of individual chemically reduced graphene oxide sheets, *Nano Lett.*, 2007, **7**, 3499-3503

7 J. T. Robinson, F. K. Perkins, E. S. Snow, Z. Wei and P. E. Sheehan, Reduced graphene oxide molecular sensors, *Nano Lett.*, 2008, **8**, 3137-40

8 B. H. Wee and J. D. Hong, A method for fabricating an ultrathin multilayer film composed of poly(*p*-phenylenevinylene) and reduced graphene oxide on aplastic substrate for flexible optoelectronic applications, *Adv. Funct. Mater.*, 2013, **23**, 4657-4666

9 R. S. Dey, S. Hajra, R. K. Sahu, C. R. Raj and M. K. Panigrahi, A rapid room temperature chemical route for the synthesis of graphene: metal-mediated reduction of graphene oxide, *Chem. Commun.*, 2012, **48**, 1787-1796

10 Z. J. Fan, W. Kai, J. Yan, T. Wei, L. J. Zhi, J. Feng, Y. M. Ren, L. P. Song and F. Wei, Facile synthesis of graphene nanosheets via Fe reduction of exfoliated graphite oxide, *ACS Nano*, 2011, **5**, 191-199

11 C. Hu, X. Zhai, L. Liu, Y. Zhao, L. Jiang and L. Qu, Spontaneous reduction and assembly

of graphene oxide into three-dimensional graphene network on arbitrary conductive substrates, *Sci. Rep.*, 2013, **3**, 2065-2075

12 J. Ning, J. Wang, X. Li, T. Qui, B. Luo, L. Hao, M. Liang, B. Wang and L. Zhi, A fast room-temperature strategy for direct reduction of graphene oxide films towards flexible transparent conductive films, *J. Mater. Chem. A.*, 2014, DOI: 10.1039/c4ta00527a

13 Y. Ye, P. Wang, E. Dai, J. Liu, Z. Tian, C. Liang and G. Shao, A novel reduction approach to fabricate quantum-sized SnO_2-conjugated freduced graphene oxide nanocomposites as non-enzymatic glucose sensors, *Phys. Chem. Chem. Phys.*, 2014, **16**, 8801-8807

14 H. B. Zhang, W. g. Zheng, Q. Yan, Y. Yang, J. W. Wang, Z. H. Lu, G. Y. Ji, Z. Z. Yu, Electrically conductive polyethylene terephthalate/graphene nanocomposites prepared by melt compounding, *Polymer*, 2010, **51**, 1191-1196

15 S. R. Stebbing, R. W. Hughes and P. A. Reynolds, Sizing, stoichiometry and optical absorbance variations of colloidal cadmium sulphide nanoparticles, *Adv. Colloid Inter. Sci.*, 2009, **147**, 272-280

16 H. Tong and Y. J. Zhu, Synthesis of CdS nanocrystals based on low-temperature thermolysis of one single-source organometallic precursor, *Nanotech.*, 2006, **17**, 845-851

17 S. S. Li, K. H. Tu, C. C. Lin, C. W. Chen and M. Chhowalla, Solution-processable graphene oxide as an efficient hole transport layer in polymer solar cells, *ACS Nano*, 2010, **4**, 3169-3174

18 I. P. Murray, S. J. Lou, L. J. Cote, S. Loser, C. J. Kadleck, T. Xu, J. M. Szarko, B. S. Rolczynski, J. E. Johns, J. Huang, L. Yu, L. X. Chen, T. J. Marks and M. C. Hersam, Graphene oxide interlayers for robust, high-efficiency organic photovoltaics, *J. Phys. Chem. Lett.*, 2011, **2**, 3006-3012

19 F. Gong, X. Xu, G. Zhou and Z. S. Wang, Enhanced charge transportation in a polypyrrole counter electrode via incorporation of reduced graphene oxide sheets for dye-sensitized solar cells, *Phys. Chem. Chem. Phys.*, 2013, **15**, 546-552

20 V. A. Marccus Martins, R. Andressa Pereira, A. s. Roberto Luz, M. Rodrigo and N. Frank Crespilho, Evidence of short-range electron transfer of a redox enzyme on graphen oxide electrodes, *Phys. Chem. Chem. Phys.*, 2013, DOI: 10.1039/c4cp00452c

21 P. Wang, T. Jiang, C. Zhu, Y. zhai, D. Wang and S. Dong, One-step, solvothermal synthesis of graphene-CdS and graphene-ZnS quantum dot nanocomposites and their interesting

photovoltaic properties, *Nano Res.*, 2010, **3**, 794-799

22 N. Zhang, M. Q. Yang, Z. R. Tang and Y. J. Xu, CdS-graphen nanocomposites as visible light photocatalyst for redox reactions in water: A green route for selective transformation and environmental remediation, *J. Catalysis*, 2013, **303**, 60–69

23 C. M. Hill, Y. Zhu and S. Pan, Fluorescence and electroluminescence quenching evidence of interfacial charge transfer in poly (3-hexylthiophene): Graphene oxide bulk heterojunction photovoltaic devices, *ACS Nano*, 2011, **5**, 942-951

24 J. G. Radich, R. Dwyer and P. V. Kamat, Cu_2S reduced graphene oxide composite for high-efficiency quantum dot solar cells. Overcoming the redox limitations of S_2^-/S_n^{2-} at the counter electrode, *J. Phys. Chem. Lett.*, 2011, **2**, 2453-2460

25 A. Xiaoqiang, Y. Xuelian, C. Y. Jimmy and Z. Guangjin, CdS nanorods/reduced graphine oxide nanocomposites for photocatalysis and electrochemical sensing. *J. Mater. Chem. A*, 2013, **1**, 5158-5164.

26 J. Wang, S. Liang, L. Ma, S. Ding, X. Yu, L. Zhou and Q. Wang, One-pot synthesis of CdS-reduced graphene oxide 3D composites with enhanced Photocatalytic properties. *Cryst. Eng. Commun*., 2014, **16**, 399-405.

27 Z. Chen, S. Liu, M. Q. Yang, and Y. J. Xu, Synthesis of uniform CdS nanospheres/graphene hybrid nanocomposites and their application as visible light photocatalyst for selective reduction of nitro organics in water. *Appl. Mater. Interfaces*, 2013, **5**, 4309-19.

28 Md. Selim Arif Sher Shah, A. Reum Park, K. Zhang, J. H. Park and P. J. Yoo, Green synthesis of biphasic TiO_2-reduced graphene oxide nanocomposites with highly enhanced Photocatalytic activity. *Appl. Mater. Interfaces*, 2012, **4**, 3893-3901.

29 P. Gao, J. Liu, S. Lee, T. Zhang and D. Delai Sun, High quality graphene oxide–CdS–Pt nanocomposites for efficient photocatalytic hydrogen evolution. *J. Mater. Chem.*, 2012, **22**, 2292-2298.

30 D. C. Marcano, D. V. Kosynkin, J. M. Berlin, A. Sinitskii, Z. Sun, A. Slesarev, L. B. Alemany, W. Lu and J. M. Tour, Improved synthesis of graphene oxide, *ACS Nano*, 4, 2010, 4806-4814

31 S. Bykkam, K. Venkateswara Rao, C. S. Chakra, V. Rajendar, R. N. Kumar and J. Ananthaiah, Graphene oxide thin films: A simple profilometer for film thickness measurement, *Int. J. Eng. Adv. Tech.*, 2013, **2**, 341-344

32 Y. Lin, J. Jie and M. Song, Preparation and characterization of covalent polymer functionalized graphene oxide, *J. Mater. Chem.*, 2011, **21**, 3455-3461

33 K. Giribabu, R. Suresh, R. Manigandan, A. Vijayaraj, R. Prabu and V. Narayanan, Cadmium sulphide nanorods: Synthesis, Characterization and their Photocatalytic activity, *Bull. Korean Chem. Soc.*, 2012, **33**, 2910-2916

34 Y. Yao, C. Xu, S. Yu, D. Zhang and S. Wang, Facile synthesis of Mn_3O_4-reduced graphene oxide hybrids for catalytic decomposition of aqueous organics, *Ind. Eng. Chem. Res.*, 2013, **52**, 3637-3645

35 M. Ivanda, K. Furic, S. Music, M. Ristic, M. Gotic, D. Ristic, A. M. Tonejc, I. Djerdj, M. Mattarelli, M. Montagna, F. Rossi, M. Ferrari, A. Chiasera, Y. Jestin, G. C. Righini, W. Kiefer and R. R. Goncalves, Low wavenumber Raman scattering of nanoparticles and nanocomposite materials, *J. Raman Spectrosc.*, 2007, **38**, 647-659

36 Z. X. Deng, C. Wang, X. M. Sun and Y. D. Li, Structure-directing coordination template effect of ethylenediamine in formations of ZnS and ZnSe nanocrystallites via solvothermal route, *Inorg. Chem.*, 2002, **41**, 869-873

37 A. Chithambararaj, N. S. Sanjini, A. Chandra Bose and S. Velmathi, Flower-like hierarchical h-MoO_3: new findings of efficient visible light driven nano photocatalyst for methylene blue degradation, *Catalys. Sci. Tech.*, 2013, **3**, 1405-1414

38 D. V. Talapin, J. H. Nelson, E. V. Shevchenko, S. Aloni, B. Sadtler and A. P. Alivisatos, Seeded growth of highly luminescent CdSe/CdS nanoheterostructures with rod and tetrapod morphologies, *Nano Lett.*, 2007, **7**, 2951-2959

39 L. Poulsen, R. Arantza Zabala, P. Steen Uttrup and P. R. Ogilby, Characterizing the behavior and properties of an excited electronic state: Electron-transfer mediated quenching of fluorescence, *J. Chem. Edu.*, 2003, **80**, 819-821.

40 P. Basudev, A. Bandyopadhyay and A. J. Pal, Molecular level control of donor/acceptor heteostructures in organic photovoltaic devices, *Appl. Phys. Lett.*, 2004, **85**, 663-665

41 S. Ameen, H. K. Seo, M. S. Akhtar and H. S. Shin, Novel graphene/polyaniline nanocomposites and its Photocatalytic activity toward the degradation of rose Bengal dye, *Chem. Eng. J.*, 2012, **210**, 220-228

42 P. Karthika, N. Rajalakshmi and K. S. Dhathathreyan, Functionalized exfoliated graphene oxide as supercapacitor electrodes, *Soft Nanosci. Lett.*, 2012, **2**, 59-66

43 S. Gunes and N. S. Sariciftci, Hybrid solar cells, *Inorg. Chem. Acta*, 2008, **361**, 581-588

Graphical Abstract

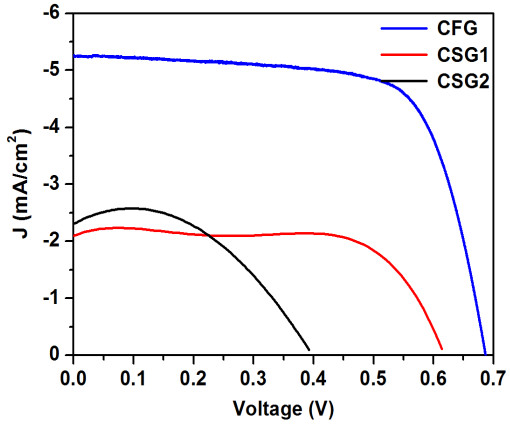

Simple surface functionalization of GO was employed with the quantum confined CdS towards the fabrication of *pn* hetero-junction based solar cell.